Computers & Fluids 90 (2014) 72–87

Contents lists available at ScienceDirect

Computers & Fluids

journal homepage: www.elsevier.com/locate/compfluid

OpenFOAM applied to the CFD simulation of turbulent buoyant atmospheric flows and pollutant dispersion inside large open pit mines under intense insolation

Federico Flores *, René Garreaud, Ricardo C. Muñoz

Departamento de Geofísica, Universidad de Chile, Santiago, Chile

ARTICLE INFO

Article history:
Received 19 March 2013
Received in revised form 9 September 2013
Accepted 7 November 2013
Available online 20 November 2013

Keywords:
CFD
OpenFOAM
Open pits
LES
Chuquicamata

ABSTRACT

The particular conditions of air circulation inside large open pit mines under intense insolation, dominated by mechanical and buoyant effects, are crucial when studying the dispersion of pollutants inside and outside the pit. Considering this, we study this problem using CFD tools able to include the complex geometry characterizing it and the different processes affecting circulation: flow interaction with obstacles, buoyancy, stratification and turbulence. We performed simulations using a previously developed *OpenFOAM* solver, focusing in the particular case of Chuquicamata, a large open pit mine (~1 km deep) located in northern Chile. Both idealized and real topographies were used. Given the importance of turbulence in this type of large-scale flows we have used LES to incorporate it in the calculation, using a DES approach to solve the flow near walls.

The results from the idealized cases support the idea that buoyant currents foster the exit of particles from the pit and increase the turbulence inside its atmosphere, modifying the purely mechanical recirculatory flow inside the cavity. Differences in the air circulation and dispersion of particles between idealized and non-idealized cases are reported. In particular, there are changes in the intensity and location of the recirculation inside the pit due to variations in the aspect ratio (length/depth) of the cavity along the axis perpendicular to the main flow. Also, the topography surrounding the mine affects the main flow that sweeps the cavity, channeling it along the main axis of the pit and forcing it to enter the cavity through the lower level of the top edge. As a consequence, the patterns of pollutant transport observed in the idealized cases, dominated by near-wall upward currents, are different than those observed in the cases with complex topography, where the dispersion is dominated by internal buoyant upward currents. Anyhow, whether by internal or near wall upward currents, in all buoyant cases considered a large percentage of the particles injected inside the pit leaves the cavity.

Further experiments studying the effect of 3D aspect ratio over the mechanically forced internal flow are needed to fully understand the effect of the internal geometry of the pit over the flow.

1. Introduction

Extraction and transport of minerals from open pit mines can produce significant emissions of fugitive dust, severely affecting the operations both inside and outside the pit. Throughout the years different techniques have been developed in order to minimize health and environmental issues, with the objective of maximizing the operations. This has increased the interest in understanding the different patterns of pollutant transport inside the atmosphere of open pit mines.

We summarize in Table 1 the main numerical studies of contaminant transport inside open pit mines. In the 1990s Baklanov was one of the first to propose the need to approach the problem from a multiphysics perspective, highlighting the combination of scales involved, and the importance of topography [1,2]. His work studied the use of ventilators to facilitate the dispersion of contaminants [3] and the effect of surface explosions on the atmosphere of the pit [4]. It verified the existence of inclined currents, defined by the topography inside the pit, controlling the dispersion of contaminants inside and around it, and detected the presence of zones of flow recirculation inside its atmosphere. Shi et al. [5] used a high resolution 3D nonhydrostatic model to simulate the air circulation inside a 2 km wide and 100 m deep pit, and were able to reproduce the intense recirculation inside the cavity, consistent with wind tunnel experiments, which was responsible for maintaining high levels of pollution inside the pit. Their results showed that both mechanical and thermal forcings are important mechanisms

* Corresponding author.
E-mail address: federico@dgf.uchile.cl (F. Flores).

0045-7930/$ - see front matter © 2013 Elsevier Ltd. All rights reserved.
http://dx.doi.org/10.1016/j.compfluid.2013.11.012

Table 1
Main numerical simulations of air circulation inside open pit mines.

Reference	Model	Pit size (*xyz*) km	Turbulence model
Baklanov [1,2], Rigina and Baklanov [4] and Baklanov and Rigina [3]	Own	$3 \times 1 \times 0.5$	Smagorinsky, $k-\varepsilon$
Shi et al. [5]	Own	$2 \times 2 \times 0.1$	$k-\varepsilon$
Silvester et al. [6]	Fluent	$1 \times 0.65 \times 0.12$	R $k-\varepsilon$

controlling the evolution of the atmosphere inside the pit, with fairly strong turbulence (maximum TKE values $\sim 2\ m^2/s^2$) produced by the interaction of both processes. Silvester et al. [6] used the CFD code Fluent to study the mechanically forced circulations developed inside the Old Moor open pit (1 km wide and 650 m deep). Without accounting for buoyancy, they showed the existense of strong mechanical shear near the top of the pit (TKE $\sim 2.5\ m^2/s^2$ in that zone), produced by the interaction of the wind that sweeps over the cavity and the internal atmosphere. These numerical experiments highlighted the importance that the geometry of the pit has over the flow (slope angle, aspect ratio, etc.), the existence of intense air flow recirculation inside the pit, and the role played by surface heat flux (that determines the intensity of buoyant currents), all factors controlling the exit of pollutants from open pits. The flow recirculation detected inside the pit by these authors is a well known phenomenon affecting flows over cavities [7–9], being the aspect ratio of the cavity (length/depth) the key parameter defining the number, size and location of the main rolls inside the cavity.

The environmental problem described before is increased in the case of very large open pit mines subject to strong insolation (annual mean surface radiation >200 W/m^2), due to the interaction between intense buoyant currents and the particular complex 3D geometry of these pits. Despite its large scale, the complex features that characterize this circulation, with developed turbulence, buoyant currents and mechanical effects due to topography, are difficult to address with standard meteorological models. There exists consensus that the problem demands appropriate inclusion of multi-physics and multi-scale processes into a Computational Fluid Dynamics (CFD) approach [10,11]. In particular, intense turbulence and recirculation induced mechanically inside the pit must be correctly simulated [5], as well as buoyancy.

In this work we focus our attention on understanding the interaction between the two main processes that control the air flow inside the internal atmosphere of large open pit mines under intense insolation: mechanical effects due to the surface geometry and convective effects due to buoyancy. Our primary target is to define the main modes of contaminant transport inside and outside Chuquicamata, a very large open pit copper mine located in northern Chile (22°17′20″S 68°54′W). Due to its large scale (width ~4 km, depth ~1 km, see Section 4) and intense insolation (the mine is located in the Atacama Desert), previous studies cannot be directly applied here.

First, we performed simulations aimed at studying the circulation using a simplified geometry, that conserves the main size of the real pit but with circular symmetry. In second place we used the complex real topography of Chuquicamata and its surroundings. The simplified geometry allows a clearer study of the processes interacting in the formation of the air circulation inside the pit, while the more realistic topography includes the effect of the real geometry. Given the great versatility that it provides, we selected the CFD tool *OpenFOAM* as development platform, using a solver previously developed [12]. We used Detached Eddy Simulation (DES), to properly simulate turbulence around complex geometries, and included density as an explicit variable in the system of equations in order to improve the treatment of buoyancy. DES combines Large Eddy Simulation (LES) far from walls, to properly solve large atmospheric eddies, and Reynolds Average Navier Stokes (RANS) techniques near walls, to solve complex geometries [13,14]. Even if the circulation inside closed valleys has been simulated in previous works [6,15,16], there is apparently no record that *OpenFOAM* has been used to study the circulation and pollutant dispersion within very large scale open pit mines subject to intense insolation. In particular, there is no evidence that the new compressible solvers that consider density as a calculation variable (instead of using the Boussinesq approximation) have been used for these applications.

Section 2 of this paper briefly describes the physical problem considered and the numerical treatment. The numerical approach used to configure the simulations was described in detail and validated in a previous work [12]. In Section 3 we present different numerical simulations using an idealized geometry similar to Chuquicamata, considering different boundary conditions in order to investigate the effect of mechanical and buoyant processes over pollutant dispersion separately. In Section 4 we describe the results of the CFD simulation of air flow inside and around Chuquicamata using its real topography, in order to identify the role played by it over the dispersion of contaminants. Section 5 includes the main conclusions taken from the work, and proposes future applications.

2. Physical problem and numerical treatment

2.1. Air circulation inside a closed valley

The air flow affecting the dispersion of pollutants inside and around closed valleys, like the ones that interest us, is composed by two main processes that control its evolution:

- Slope flows controlled by buoyancy, which will generally be the flow dominating the circulation inside the pit. There exist several references relative to this type of flows [17–19].
- Mechanical effects produced by the interaction of the external flow with the geometry of the cavity. The approximately conical features of open pit mines modify the circulation imposed by buoyant slope flows, introducing mechanical effects produced by the slope angle and circular symmetry of the pit. In this regard, the analysis is similar to that developed for valleys [20,21], although the open condition of the latter allows for exit flows not possible in closed pits. Given that the existence of large scale closed valleys is rare in nature the research about air circulation inside their atmosphere has remained restricted to meteoritical craters, or to the specific case of large open pit mines [6,22].

2.2. Numerical approach

2.2.1. Model

We have already described in [12] the numerical approach used in our simulations, as well as its validation against documented data. The solver includes the following equations: continuity, momentum conservation (Navier–Stokes), enthalpy conservation, ideal gas state and passive scalar transport, using the libraries

and tools provided by *OpenFOAM* to solve them (thermophysical, turbulence and finite volume libraries). We have chosen a numerical approach that includes density as an explicit variable in the system of equations, instead of using the Boussinesq approximation. The density-based non-Boussinesq formulation used to solve buoyant flows in *OpenFOAM* includes density as an explicit variable in the calculation and uses PISO type algorithms (Pressure-Implicit with Splitting of Operators) to couple pressure and velocity in the compressible case. A detailed view of PISO type compressible algorithms can be found in [23–26]. We use a DES (Detached Eddy Simulation) approach to solve the flow near walls, in order to be able to include complex topography (Spalart–Allmaras DES formulation). LES (Large Eddy Simulation) is used to solve the turbulent eddies far from walls. Results obtained in [12] showed that the model and the particular boundary and initial conditions implemented in *OpenFOAM* for this work can deal with the complex multiphysical problem that implies modeling atmospheric buoyant flows close to a complex ground. DES allows us to use the advantages offered by LES when modeling turbulent atmospheric flows, without having to pay the high computing cost that would be implied by using this technique in complex geometries.

2.2.2. Geometry and meshing

As in the previous work [12] we used the *snappyHexMesh* toolbox to generate the mesh, in conjunction with the CAE software *Salome* to create the necessary STL files. *GlobalMapper*, a mapping software package, was used to create STL files from real topography (SRTM data). *Matlab* was used to modify the files generated by *GlobalMapper* to allow their use by *snappyHexMesh*.

2.2.3. Computing support

The configuration of the simulations and the analysis of their results was done on a personal workstation using *Paraview*, while their execution was done in parallel in the Levque cluster of the National Laboratory for High Performance Computing (NLHPC) of the Center for Mathematical Modeling of the University of Chile. The Levque cluster is an IBM iDataplex machine with 536 cores, equipped with Intel Nehalem processors, an Infiniband QDR switch and several development tools [27].

3. Idealized cases

3.1. Domain

In this first part we used a simplified topography, that retains the same general dimensions of Chuquicamata (see Section 4), representing the pit as an inverted truncated cone with a superior diameter of 4 km, an inferior diameter of 1 km and 1 km deep (Fig. 1b). We selected this simplified symmetric geometry since it allows a clearer study of the processes interacting in the formation

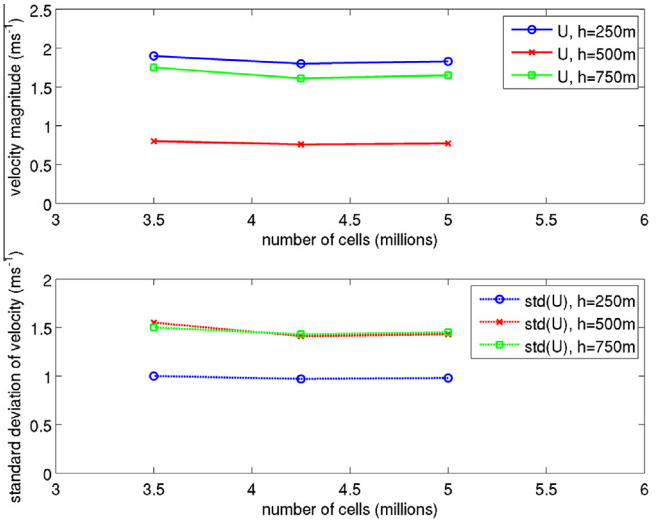

Fig. 2. Example showing the variation of mean velocity and standard deviation of velocity at three single points, used to study mesh independence. The points are located at the center inside the pit, at 250 m (blue), 500 m (red) and 750 m (green) above the bottom. (For interpretation of the references to color in this figure legend, the reader is referred to the web version of this article.)

of the air circulation inside the pit. The simulation domain consisted of a rectangular region 15 km long, 10 km wide and 3 km high (Fig. 1a). Although the domain is small, considering the size of the cone, it was chosen after several mesh tests produced solutions independent of domain size and mesh (Fig. 2). Due to the high computational cost of this kind of simulations a balance must be reached between domain size and mesh resolution. The *snappyHexMesh* tool was used to generate the mesh based on a STL file created using *Salome*, providing a mesh with nearly 5 million cells. The mesh was refined near walls, by the use of *snappyHexMesh* controls, to produce cells with wall normal dimensions of between $y_1^+ = 100$ and $y_1^+ = 1000$ adjacent to the surface (y_1^+ is the distance in wall units between the centroid of the first cell and the wall assuming the y coordinate is normal to the wall). However, it is impossible to satisfy this criterion everywhere when processes of flow separation and attachment occur. The refinement procedure produced vertical grid spacing on the order of meters near the ground, tens of meters below 1500 m above the top edge of the pit, and hundreds of meters above (the top of the convective boundary layer is located ~1000 m above the top edge of the pit).

3.2. Experimental setup

We employed cyclic lateral boundary conditions in both horizontal directions. The upper boundary conditions (2 km above

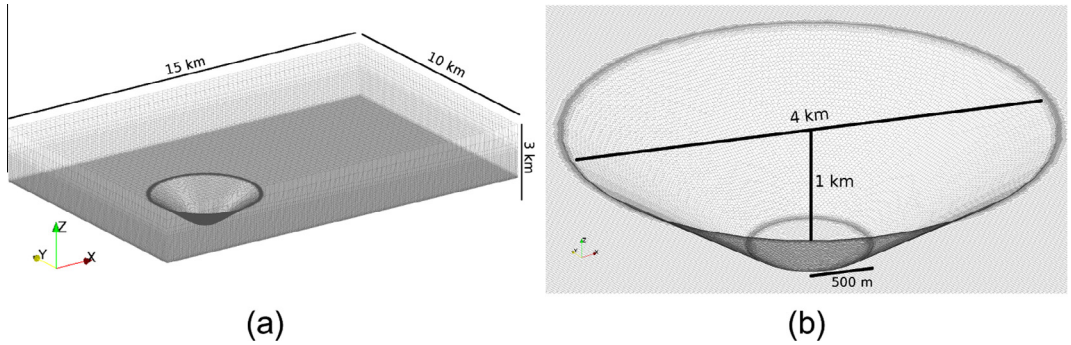

Fig. 1. Mesh used. (a) Total domain and (b) detail, inverted cone.

the top edge of the pit) are free-slip and maintain a constant potential temperature gradient. The initial potential temperature profile has a constant value of 300 K up to 937 m above the top edge of the pit (all the internal volume of the cone has constant potential temperature), followed by an 8 K increase in the next 167 m, and a constant 0.003 K/m gradient up to the top of the domain (as used by Moeng and Sullivan [28] and Churchfield et al. [29]).

Because of our interest in studying the interaction between buoyancy and mechanical effects, we defined three numerical experiments in which these processes have different relative importance. A summary of the cases and the designation codes is shown in Table 2. The first case, W, is dominated by winds aloft (10 m/s at 300 m over the top edge of the pit, vertical profile following a power law as described in [12]), and does not consider any thermal effect (no enthalpy equation included, neutral atmospheric boundary layer). Case B is dominated by buoyancy, with a surface heat flux of 240 W/m^2, and only a 1 m/s wind speed 300 m above the top edge of the pit. The third case, WB, combines both previous cases, keeping a 10 m/s wind aloft and a 240 W/m^2 surface heat flux.

In order to facilitate the initial development of turbulence, the initial velocity field was perturbed as suggested by de Villiers [30], introducing periodic perturbations along the x and y-axes through sine and cosine functions. The time step used in each simulation was 0.025 s, necessary to keep a low Courant number near the surface where the mesh is refined, for a full simulation time of 2 h (until reaching a statistically stationary flow). To determine whether the steady state was achieved we performed time statistics while the simulation was executing in order to test the evolution of the temporal means of velocity (time evolution of the moving-average of the velocity at different points inside the domain). Also, different final times have been tested to ensure that convergent time-averaged results were attained. As a reference for monitoring statistical convergence in LES simulations see for example [31]. In each idealized case around one month of CPU time was necessary in Levque cluster, running in parallel in 32 cores (Intel(R) Xeon(R) CPU X5550 (Nehalem) 2.67 GHz). For further details of the numerical approach used see [12].

3.3. Results

In order to analyze the circulation imposed by each case and its effect on the dispersion of contaminants inside and around the pit, we use two simple techniques to visualize this circulation. First, we use time-averaging over the last hour of simulation to describe the mean patterns of circulation. Then, injecting passive tracers to the velocity field, we study the features that characterize the currents leaving the pit, in such a way that we can explore the dispersion of contaminants emitted from the surface.

3.3.1. Mean values

The last hour mean vector velocity field is presented for each case in Fig. 3. Panels 3a, c and e show a vertical plane that runs through the center of the pit, while panels 3b, d and f show a horizontal plane 250 m above the bottom of the pit (height scale indicated in the vertical plane). The existence of distinctive circulation patterns in each case can be observed. In both cases with positive surface heat flux (B, panels 3c and d and WB, panels 3e and f) the air circulation inside the pit is characterized by strong convective currents (vertical velocity >2 m/s) that ascend close to the walls. In case W (panels 3a and b), in which the wind dominates, there are no clearly defined ascending currents close to the walls. Two flow features can be identified in this case: a circulation that follows the geometric pattern of the pit, with convergent currents near the downwind slope, induced by circular symmetry (the flow near the top edge of the pit follows the circular walls of the cavity, feature not seen in the vertical plane but visible in a horizontal plane near the top edge (not shown) and in Fig. 3 counter-direction flow inside the pit (as reported in previous works [1,5]), which induces descending flow in the downstream wall and ascending flow in the upstream wall. Flow separation occurs at the top of the upstream wall, induced by local changes in pressure [32]. The vorticity present near ground (no-slip boundary) evolves into a large eddy when the boundary condition changes [33]. This eddy is not clear in Fig. 3a, mainly due to vector scale and symmetry. Descending currents closing the eddy are very weak (~0.5 m/s) compared to the main wind aloft (~10 m/s). Also, the main eddy is more evident outside the symmetry plane shown in Fig. 3a, since it developes mainly near the walls outside that plane. The circular geometry of the pit reduces the aspect ratio of the cavity along the y-axis (perpendicular to the main flow) outside the vertical symmetry plane, favoring the formation of a more intense eddy near the lateral walls [8] (a well defined eddy is visible in a vertical plane 300 m outside the symmetry plane, Fig. 4). Fig. 3c and d (case B) show the recirculation produced by the interaction between upslope flows and the weak incident ambient wind, and the presence of vertical convective currents inside the pit near ground (below 300 m). In this case wall updrafts seem to be the more relevant flow, with compensatory subsidence inside. The effect of upslope currents is less important in case WB (Fig. 3e and f), affected also by 10 m/s wind, in which the mean circulation seems to be a combination of both previous cases. In this case the main internal eddy shows a clear structure, and seems reinforced by buoyant currents.

Fig. 5 shows the standard deviation of velocity magnitude in all cases. In case W (Fig. 5a) intense turbulence occurs near the top of the pit due to the interaction between the flow aloft and the internal atmosphere. In case B (Fig. 5b) the turbulence is linked to thermal updrafts, while in case WB (Fig. 5c) turbulence increases its magnitude and extends inside all the pit. As shown in Fig. 3, buoyancy increases the recirculation induced by the incident wind, increasing the circulation and turbulence inside the pit.

3.3.2. Tracking of particles

Given our interest in studying the dispersion of pollutants from the interior of the pit we used tracking of particles to analyze air circulation. Using the *Paraview* software we injected instant puffs of 18,000 particles in an imaginary 500 m diameter disc 10 m above the bottom of the pit (radial resolution: 50 particles, circumferential resolution: 360 particles), every 50 s, during the last hour of simulation. The particles are treated as ideal tracers, with no sedimentation velocity. A video showing the evolution of these particles exposes the differences between each case (video link), and Fig. 6 shows the final locations of the injected particles (at the end of the second hour), the color indicating the original location of each particle (red $-y$, blue $+y$).

In cases B and WB a large number of particles leaves the pit, while in case W only a small fraction of the injected particles leaves the cavity, after a long time since their injection, due to the recirculation effect, as suggested by previous studies [5,6]. The role of wind becomes clear comparing scenarios B and WB, especially the top views 6d and f. In case WB (10 m/s wind), with

Table 2
Idealized cases. Wind speed is specified 300 m above the top edge of the pit.

Predominance	Name	Wind above 300 m	Surface heat flux
Wind	W	10 m/s	0
Surface heat flux	B	1 m/s	~240 W/m^2
Wind and surface heat flux	WB	10 m/s	~240 W/m^2

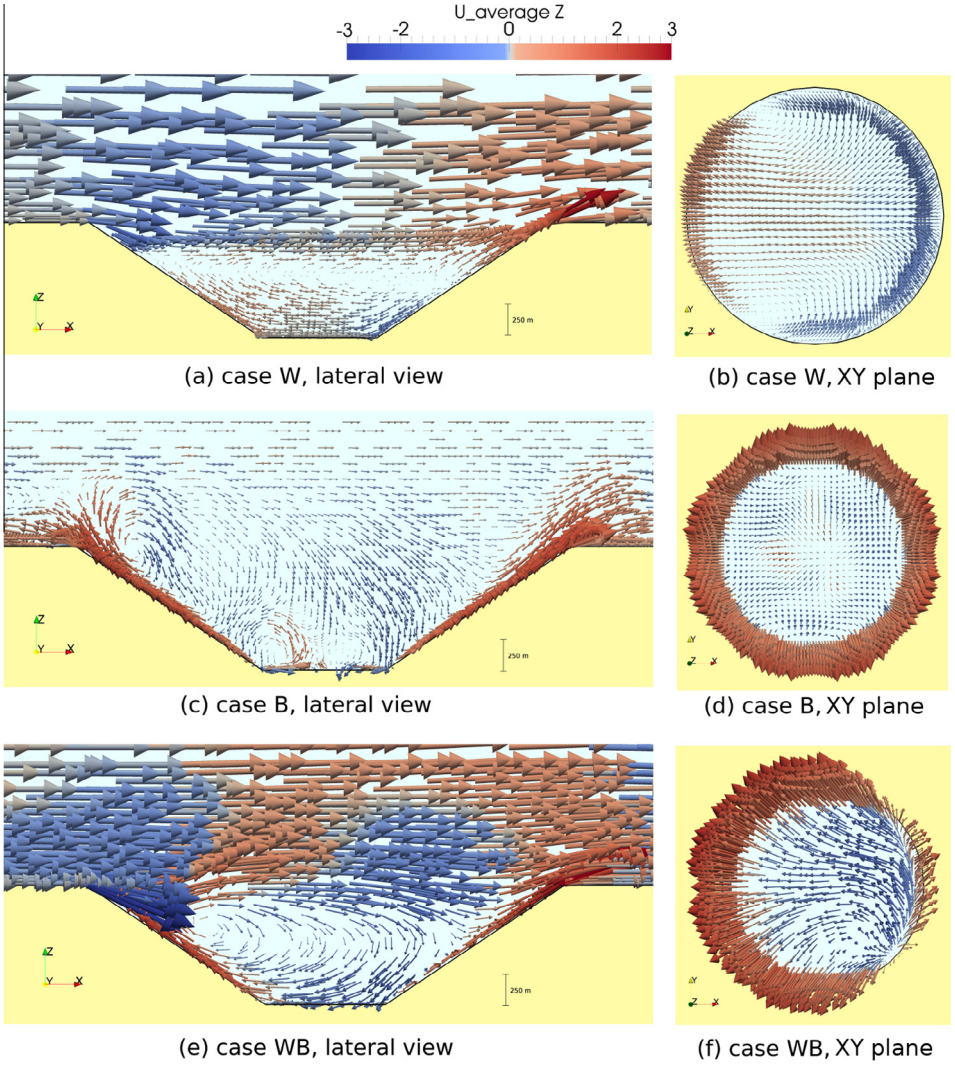

Fig. 3. Mean vector velocity field during the last hour of simulation, for each case. (a), (c) and (e), Vertical plane in the middle of the basin ($y = 0$). (b), (d) and (f), Horizontal plane 250 m above the bottom of the pit. Color indicates mean vertical velocity (color bar, m/s). Vector scale is the same for all cases. (For interpretation of the references to color in this figure legend, the reader is referred to the web version of this article.)

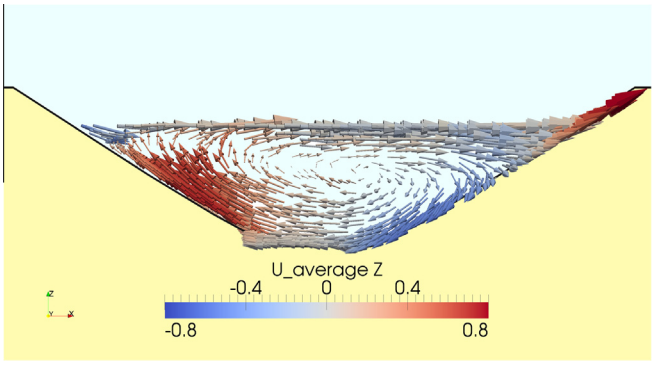

Fig. 4. Mean vector velocity field during the last hour of simulation for case W. Vertical plane 300 m outside the symmetry plane. Vector scale is not the same of Fig. 3. We have increased it and eliminated the vectors above the pit in order to improve the visualization of the main roll. Color indicates mean vertical velocity (color bar, m/s). (For interpretation of the references to color in this figure legend, the reader is referred to the web version of this article.)

stronger wind than in case B (1 m/s wind) the particles, once they reach the top edge of the pit, are dragged downstream. In case B on the contrary, particles leaving the basin close to the walls accumulate over the top edge, especially upstream, where convective currents interact with the weak incident wind (recirculation at the upstream top edge seen in Fig. 3).

Fig. 7 shows the temporal evolution of the injected particles. Only the final location of three puff of particles is shown: blue dots mark the final locations of particles released 30 min before end time, green dots those released 20 min before end time and red dots those released 10 min before end time. In case W (Fig. 7a and b) the intense recirculation inside the pit drags the particles toward the upwind slope, producing their uplift, but not enough to reach the edge. Even oldest particles stay inside the pit, but are affected by the turbulent flow present at the top of the cavity, where the incident wind aloft interacts with the internal atmosphere (Fig. 6a), extracting some of the particles. In case B (Fig. 7c and d) the temporal evolution of particles is influenced by convective currents, present both in the center of the basin and near the walls, where they are stronger (vertical velocity ~2.5 m/s near the walls, ~1 m/s in the center). Older particles (blue), that have had the time necessary to reach the walls, have been expelled out of the pit. Particles with shorter lifetime (green and red) are dominated by internal thermal lifts and remain near the center of the basin. In this case upward currents following

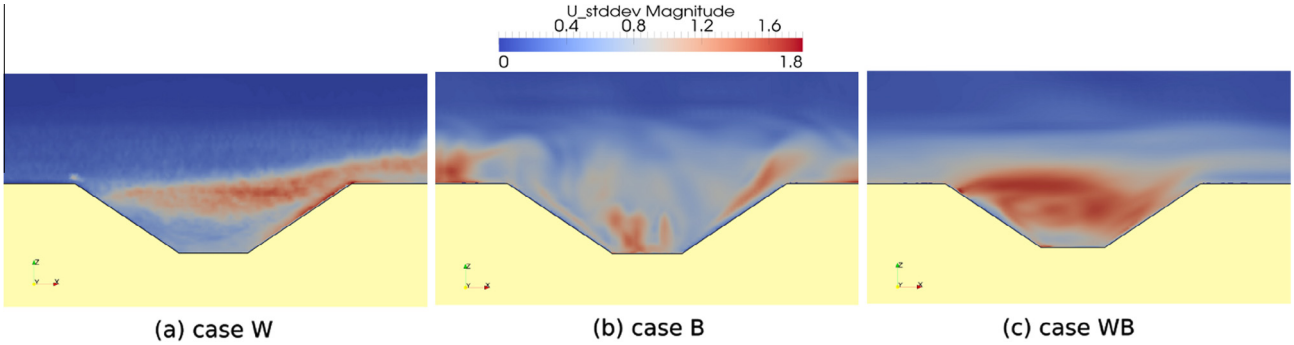

Fig. 5. Standard deviation of velocity magnitude (m/s). (a) Case W, (b) case B and (c) case WB.

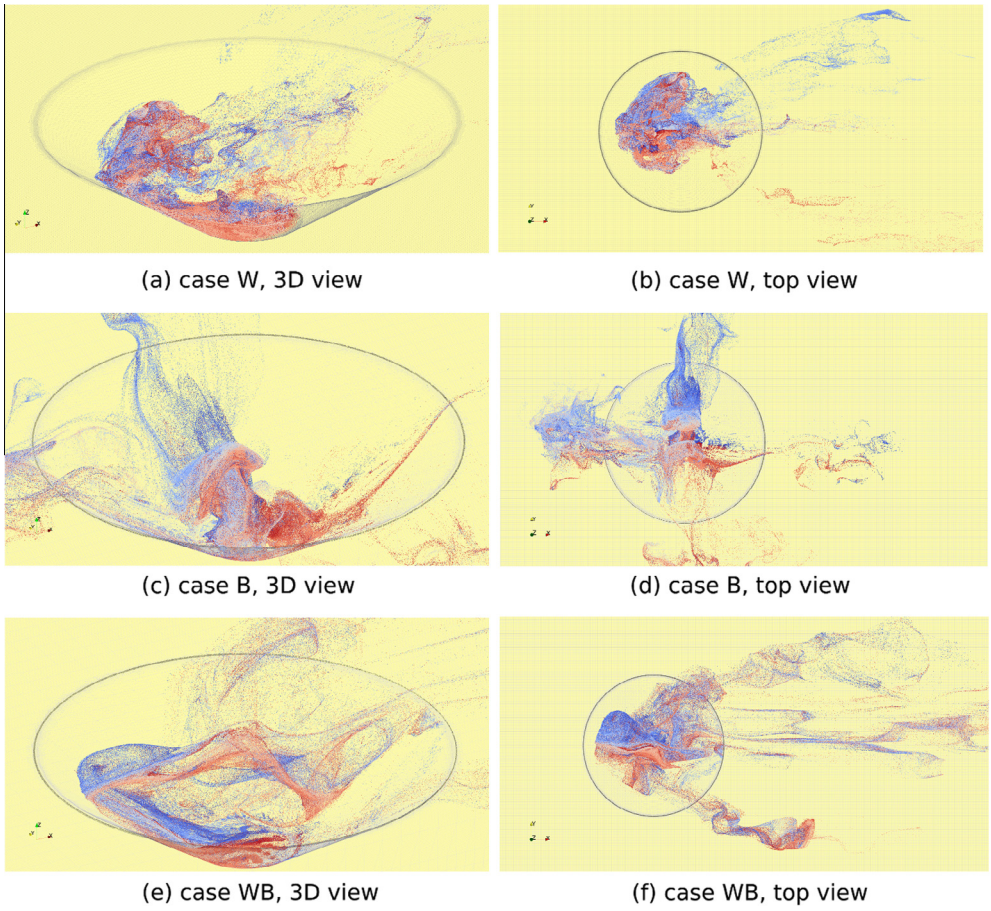

Fig. 6. Location of bottom injected particles at final time. Color indicates the original location of each particle (red $-y$, blue $+y$). (For interpretation of the references to color in this figure legend, the reader is referred to the web version of this article.)

the lateral walls are preferred by the particles leaving the pit, probably due to descending currents induced by recirculation and compensatory subsidence (Fig. 3c). The 10 m/s wind present in case WB (Fig. 7e and f) changes the patterns described above. In this scenario the thermal lifts at the center of the basin are less important, probably due to the recirculation induced by the external wind, perturbing air circulation inside the pit and approaching released particles to the upwind slope (left wall in figure). This process increases the number of particles that reach the top edge of the pit and reduces their lifetime near ground (red particles). The recirculatory flow induced by the interaction between the wind aloft and the internal atmosphere is shown by green particles that are mixed in that zone (Fig. 7e). In this case the convective currents speed up the evolution of particles, accelerating the processes observed in case W. Air recirculation inside the pit facilitates the approach of particles to the upwind slope, accelerating their exit of the pit. At the same time this recirculatory flow produces that some of the particles that have risen re-enter into the basin, while others go downstream following the winds aloft. Then, even if the wind accelerates the exit of particles, approaching them to convective currents near walls, it also contributes to their re-entry into the pit.

Fig. 8 quantifies the percentage of particles remaining inside the pit after a given time since their injection (lifetime). In this case we injected a single puff of 18,000 particles at the beginning of the last hour at different locations: a horizontal disc 10 m above the bottom of the pit as the previous one (black lines in Fig. 8), 50 m-wide ring at 250 m above the bottom with its outer perimeter touching

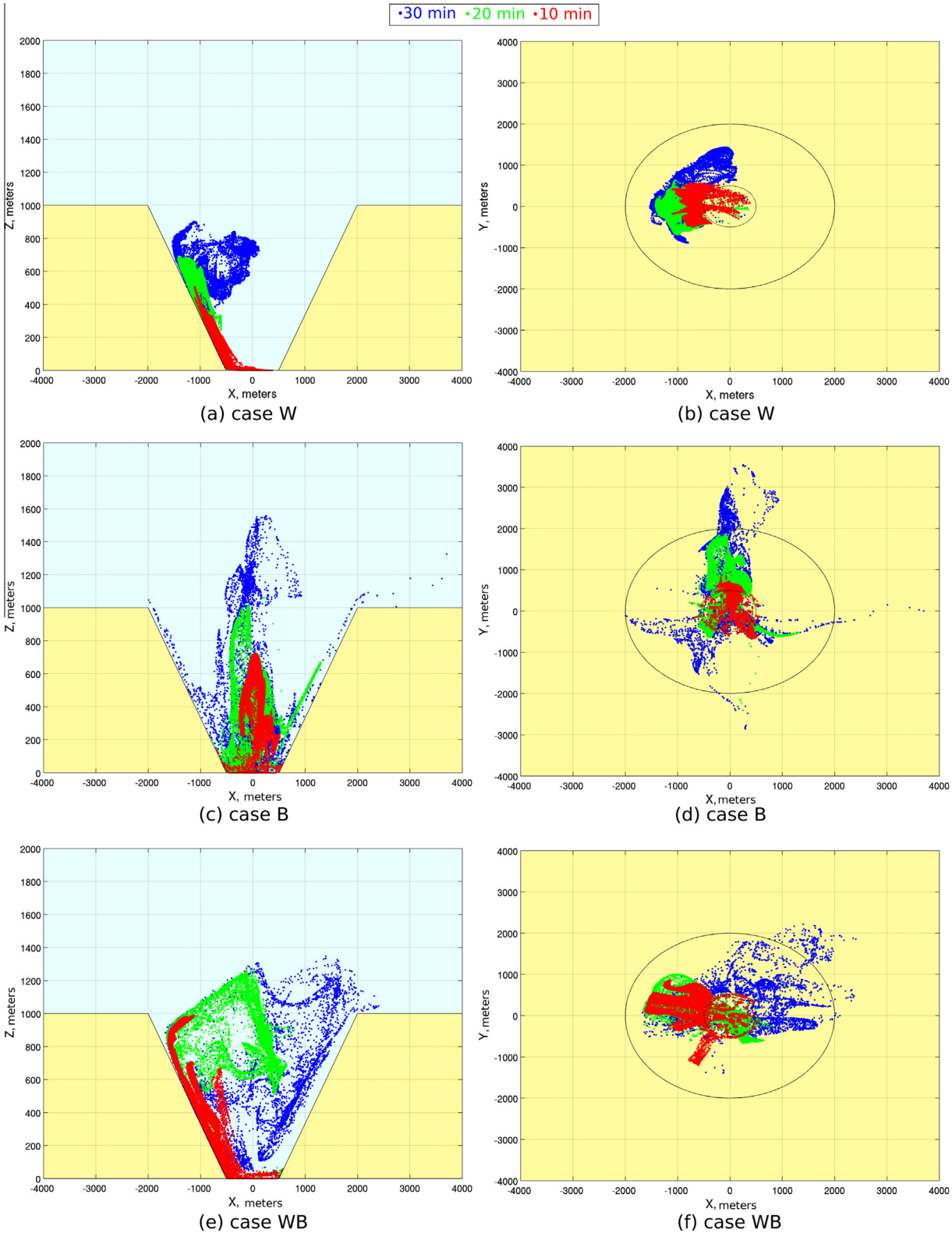

Fig. 7. Final locations of particles released 30 (blue), 20 (green) and 10 (red) minutes before end time. (a) and (b) Case W. (c) and (d) Case B. (e) and (f) Case WB. These are not section views, all particles in 3D space are included. (For interpretation of the references to color in this figure legend, the reader is referred to the web version of this article.)

the surface of the slope of the pit (blue lines), a similar ring at 500 m (green lines) and another one at 750 m (red lines). In case W the percentage of particles inside the pit decreases slowly. Some particles, due to the intense recirculation inside the cavity, are able to reach the top edge of the pit and exit the cavity driven by the wind aloft. In this case, particles injected in a disc near the ground (black line) follow a counterintuitive behavior: their discharge is faster than those of particles injected in a ring at 250 m. This could be related to recirculation: particles injected at 250 m near the downstream wall are forced to descend before their exit following

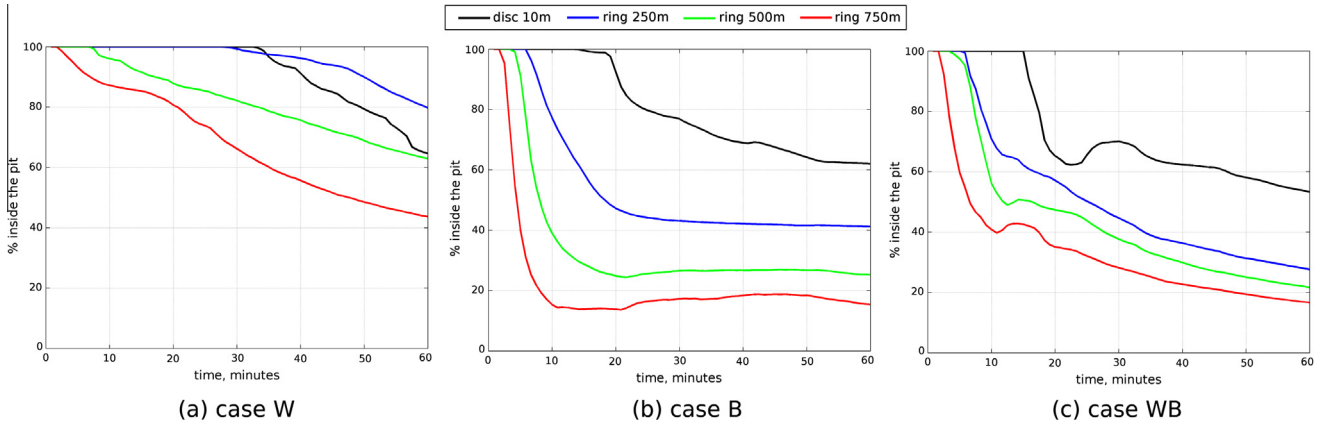

Fig. 8. Percentage of a puff of particles injected at different levels that remains inside the pit v/s time. (a) Case W. (b) case B. (c) Case WB. Black line, 500 m diameter disc at 10 m from the bottom; blue line, 50 m-wide ring at 250 m; green line, ring at 500 m; red line, ring at 750 m. (For interpretation of the references to color in this figure legend, the reader is referred to the web version of this article.)

the upstream flow along the upstream wall, while particles injected in a disc near the ground are swept by internal counter-direction flow (Fig. 3b). In case B (Fig. 8b), affected by strong convective currents (vertical velocity ∼2 m/s) and weak wind (1 m/s), the percentage of particles injected in a ring that remains inside the pit drops quickly, depending on the altitude of injection. This fast discharge is related to the upward currents close to the walls of the pit. In this same case the discharge of particles injected in a disc close to the bottom of the pit is slower, and takes also a large amount of time to begin. As we already saw, this can be related to the time required by the particles released at the center of the pit to approach the upward currents near the walls. The quasi-steady state reached could be attributed to particles that are not able to exit the pit due to subsidence inside its atmosphere. In case WB (Fig. 8c) the effect of recirculation induced by the stronger wind aloft (10 m/s in case WB against 1 m/s in case B) is responsible for an abrupt change in the rate of discharge, initially similar to that of case B. There is also a reduction in the time needed to initiate the exit of particles injected at the disc near the bottom of the pit. The differences between both cases can be attributed to the recirculation enhanced by the stronger wind in case WB (10 m/s in case WB against 1 m/s in case B), which favors the entry of particles inside convective currents, accelerating their initial output, but also inducing their re-entry to the pit. In fact, as shown in Fig. 8b and c, particles injected at the upper ring discharge faster in case B than in case WB, while those injected at the bottom ring discharge faster in case WB than in case B.

3.4. Conceptual model

A simplified conceptual scheme is presented in Fig. 9 for each idealized case. In case W (Fig. 9a) the main flow aloft induces recirculation inside the pit. This is a well known pattern of the flow over open cavities [7–9]. The magnitude and location of the main roll inside the cavity is a function of the geometry, particularly, the aspect ratio of the cavity (length/depth). The aspect ratio changes the number, location and magnitude of the eddies inside the cavity (see for example Fig. 2 in [8] and 6 in [9]). In this case the geometry of the pit mainly coincides with a 4:1 aspect ratio, although its conical feature enhances upward and downward currents near the walls, while its circular geometry produces changes in the aspect ratio along the y-axis. Both factors slightly modify the patterns seen in [8], where the main eddy inside the pit is located closer to the downstream wall than in this case. Also, as previously described, in our case the structure of the main roll is more clearly defined outside the vertical symmetry plane, since the walls outside the symmetry plane, where the aspect ratio is smaller, highly contribute to the recirculation. Strong turbulence exists at the top of the pit (standard deviation of velocity magnitude ∼1.6 m/s), enhancing the exit of particles that reach that zone carried by ascending currents linked to the main roll. In case B (Fig. 9b) strong convective currents near the walls (vertical velocity >2 m/s) dominate the flow. The interaction between the low incident wind aloft and the convective updraft leaving the pit upstream generates a roll near the top edge of the pit (similar to that seen over cavities). This roll blocks the influence of the weak main flow over the rest of the atmosphere inside the pit. The strong currents leaving the pit (vertical velocity >2 m/s) induce, by continuity, descending flow at the center of the cavity. However, due to the intense heat flux at the base, convective updrafts at the center of the pit remain, overcoming the descending flow near the base. In case WB (Fig. 9c) both schemes described above combine. The 10 m/s incident wind is able to overcome the convective current at the upwind wall and generate a roll inside the pit similar to that seen in case W. This roll changes its location and intensity, becoming more intense and approaching the upwind wall. This displacement leaves a wide area of descending flow near the center of the pit, that compensates the intense convective upward currents. The intensity of the main roll sweeps all the convective updrafts near the base at the center of the pit. In this case the effect of buoyancy is similar to changing the aspect ratio of the pit (roll similar to 1:1 aspect ratio cavities [8]). In case W the exit of particles is mainly produced by the intense turbulence at the top levels inside the pit: upslope currents produced mechanically near the upstream wall carry the particles near the top edge, where some of them leave the pit due to the intense turbulence in that zone. In case B the exit of particles is controlled by convective currents near walls, while in case WB the upslope convective current near the upstream wall dominates: recirculation inside the pit sweeps the particles approaching them to the upstream wall, where an intense upslope current carry them to the top edge. There, some of them leave the pit directly and others enter the zone of intense turbulence as in case W.

4. Real topography

Chuquicamata is an open pit copper mine located in northern Chile (western slope of the Andes, 22°17′20″S 68°54′W, ∼3000 m altitude, Fig. 10a), whose vast dimensions make it one of the largest pits in the world, with more than 4 km long, 3.5 km wide and almost 1 km deep (Fig. 10b). Due to its location in the Chilean desert,

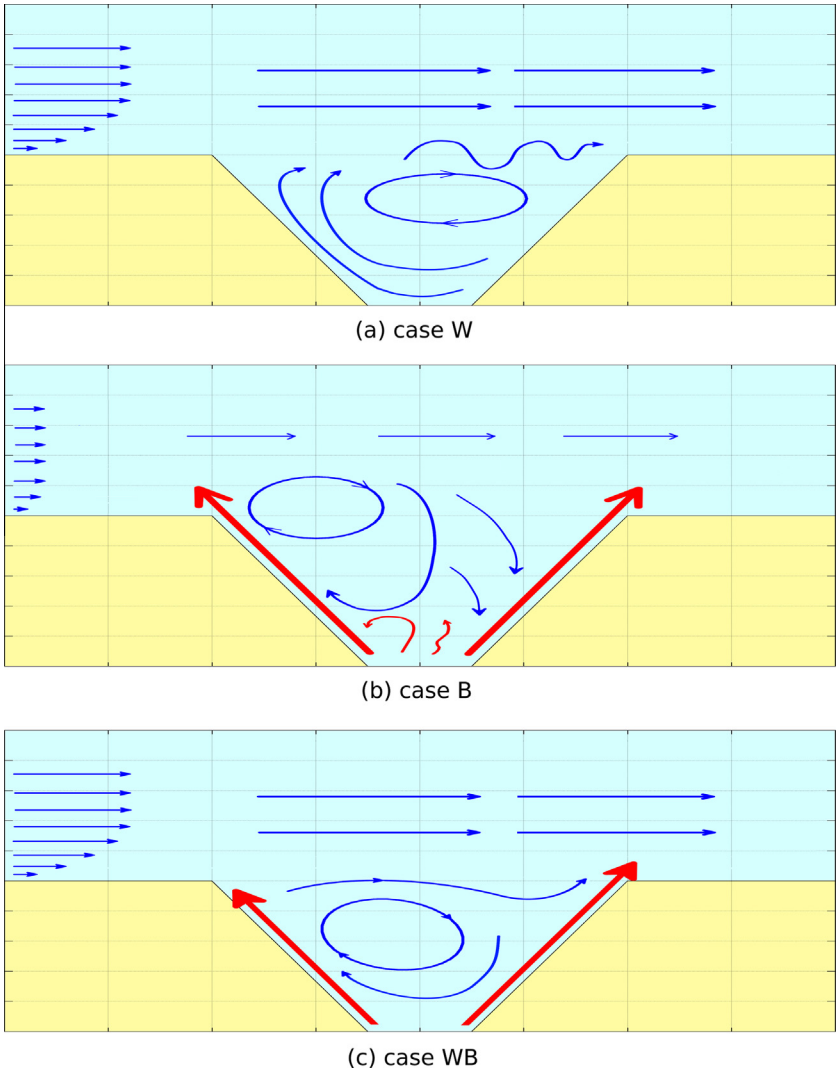

Fig. 9. Simplified conceptual scheme of the flow. (a) Case W. (b) Case B. (c) Case WB. Geometrical scales were modified to improve representation. Vectors are not at scale. In red, convective currents. (For interpretation of the references to color in this figure legend, the reader is referred to the web version of this article.)

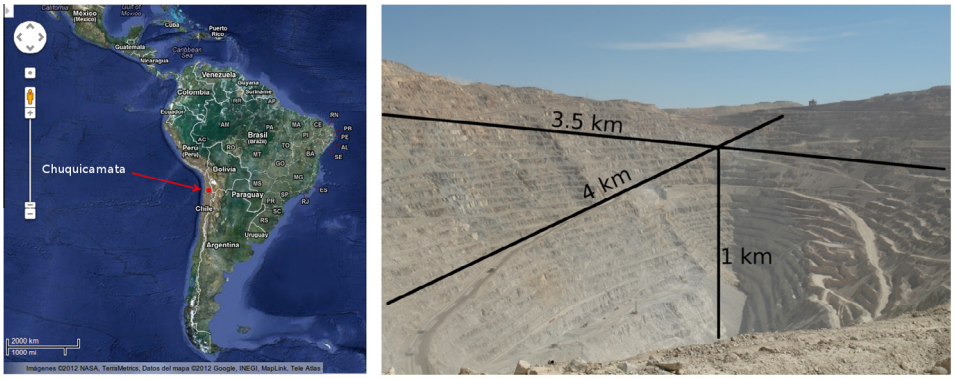

Fig. 10. (a) Location of Chuquicamata, (b) Chuquicamata open pit, most relevant dimensions (©Codelco, Chilean National Copper Corporation, under Creative Commons).

Chuquicamata is exposed to high rates of solar radiation all the year (200–350 W/m^2 annual mean surface radiation [34]), fostering the generation of convective currents inside its atmosphere. Due to operations undertaken inside the pit (movement of machinery, blasting), and the type of soil, fine powder streams are almost always present, generating an environmental problem both inside and outside the pit. The transport of these particles follows a diurnal cycle, influenced by convective currents that promote their dispersion during day [34]. Due to its geographic location, the wind over Chuquicamata is affected by the regional circulation over the Pacific and the Andes cordillera. The upper-level large-scale circulation is characterized by moderate easterly wind at low latitudes

(±15° of latitude) and westerly winds at subtropical/extratropical latitudes [35]. Due to its altitude (~3000 m a.s.l.) and latitude (22°17′20″S) the mean wind conditions above Chuquicamata are affected by this westerly circulation [36,37]. In fact, the data from a weather station in Calama, the nearest city to the pit (located about 13 km southwest of the mine), shows a predominance of westerly wind during daytime/summer, while easterly wind predominates during nightime/winter. Both patterns are driven by heating/cooling of the Andean slope and the large-scale westerlies. For detailed information see for example the data from Chilean Weather Service (DMC), available at http://www.meteochile.gob.cl/.

4.1. Domain

The topography around Chuquicamata is complex, especially to the west of the pit. Considering that the large scale predominant wind direction during day is westerly, to correctly simulate the flow affecting the pit the complex topography at its west must be incorporated in the domain. As the configuration of our simulations uses cyclic boundary conditions (to correctly simulate the flow of heat and avoid compressibility problems), the domain and mesh generation of this case is particularly complex. To solve this problem we selected the domain in such a way that both inlet and outlet boundary topographies are similar, and as simple as possible (Fig. 11a), using SRTM data and *GlobalMapper* to create an elevation data file. Then, we modified the file created by the software to include inlet and outlet transition zones at the same level with flat topography (we included different levels until reaching the same level at both boundaries), in order to allow the creation of well defined inlet and outlet cyclic boundaries. Finally, we used again *GlobalMapper* to create the necessary STL file. As expected, this technique highly increases the computational cost of the simulation, increasing the number of cells of the domain, but it allows the inclusion of the complex topography upwind of the pit, in order to run a more realistic simulation. The *snappyHexMesh* tool was used to generate the final mesh based on the STL file, pro-

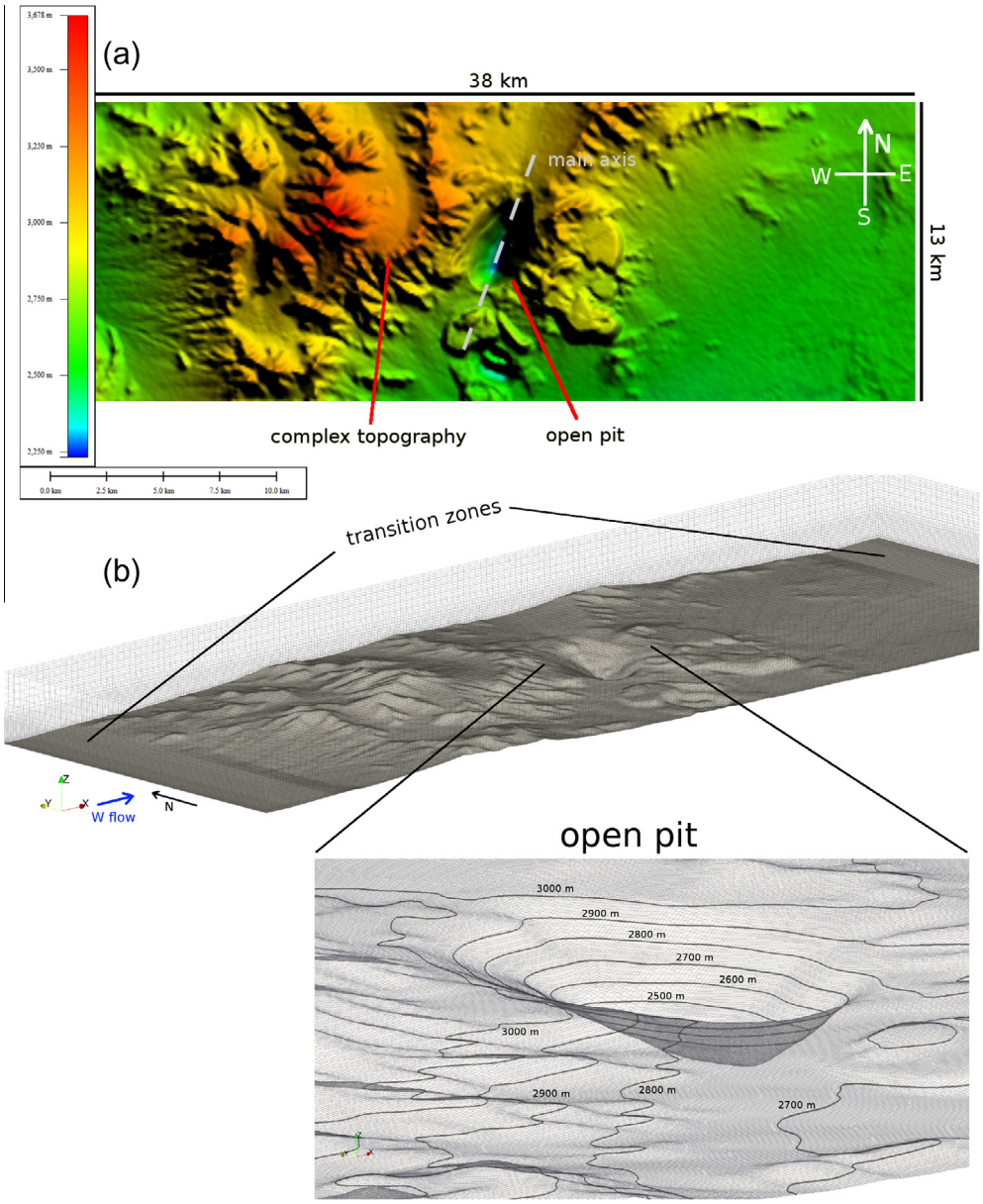

Fig. 11. (a) Topography from *GlobalMapper*. Color bar represents height above sea level. Hills block the inlet flow at the west of the mine. The main axis of the pit is tilted ~15° from north. Size of the domain included. (b) *OpenFOAM* mesh, includes inlet and outlet transition zones. Detail of the pit includes topographic contour lines (only contours over 2500 m are visible). (For interpretation of the references to color in this figure legend, the reader is referred to the web version of this article.)

viding a mesh with nearly 7 million cells (Fig. 11b), refined near walls to produce cells with wall normal dimensions of between $y_1^+ = 200$ and $y_1^+ = 5000$ adjacent to the surface. However, it is impossible to satisfy this criterion everywhere when processes of flow separation and attachment occur. The refinement procedure produced vertical grid spacing on the order of meters near the ground, tens of meters below 1500 m above the top edge of the pit, and hundreds of meters above (the top of the convective boundary layer is located ~1000 m above the top edge of the pit). Fig. 11 also shows a detail of the pit included in the mesh. Topographic contour lines are included as reference to highlight the complex topography and the detail required by the mesh, refined close to the terrain. Several mesh tests were performed until obtaining solutions independent of domain size and mesh.

The main differences between the more realistic topography used here and the idealized geometry used in the previous section are the following:

- *Asymmetry*. The real topography shows a clear main axis, especially at the bottom layers inside the pit (Fig. 11), tilted ~15° from north. As a consequence, the base area is much larger than in the idealized case (~2.5 km against ~1 km), eliminating the circular symmetry near ground.
- *Top edge irregularity*. The top edge of the real pit is mostly irregular, with different heights depending on location (top edge between 700 and 1000 m above the bottom of the pit).
- *Irregular walls*. Real hillsides are perturbed by several irregularities, changing their slope angle along the interior of the pit.
- *Surroundings*. Hills surround the real pit, particularly at its west (highest peaks reach ~600 m above the top edge of the mine).

4.2. Initial and boundary conditions

We employed cyclic inlet and outlet boundary conditions in the west–east direction. To simplify the mesh generation and limit the size of the domain we did not include cyclic lateral boundaries in the south–north direction, as we imposed a west–east forcing flow (lateral boundaries are defined as inviscid wall: normal component and gradients of tangential components of velocity equal zero). The upper boundary conditions are free-slip and maintain a constant potential temperature gradient. The initial potential temperature profile has a constant value of 300 K up to 937 m above the top edge of the pit (including its internal volume), followed by an 8 K increase in the next 167 m, and a constant 0.003 K/m gradient up to the top of the domain (as used in the idealized cases and in [28,29]). We simulated two cases, with 3 and 10 m/s wind speed

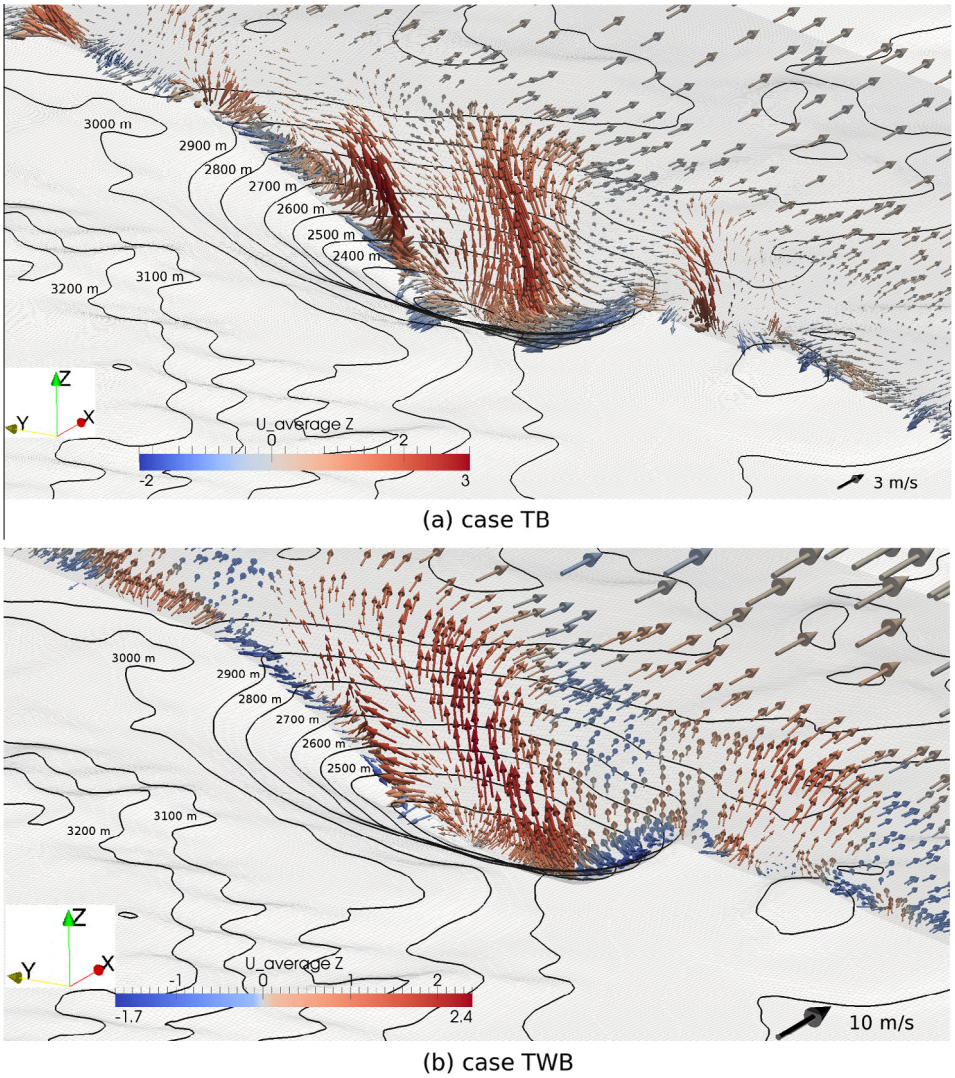

Fig. 12. Last hour mean velocity vector field in a plane aligned with the main axis of the pit (see Fig. 11). (a) Case TB, wind aloft 3 m/s. (b) Case TWB, wind aloft 10 m/s. Color bar associated to vertical velocity U_z, m/s. Topographic contour lines included. To improve visualization a different vector scale was used in each case, due to the difference in wind magnitude. (For interpretation of the references to color in this figure legend, the reader is referred to the web version of this article.)

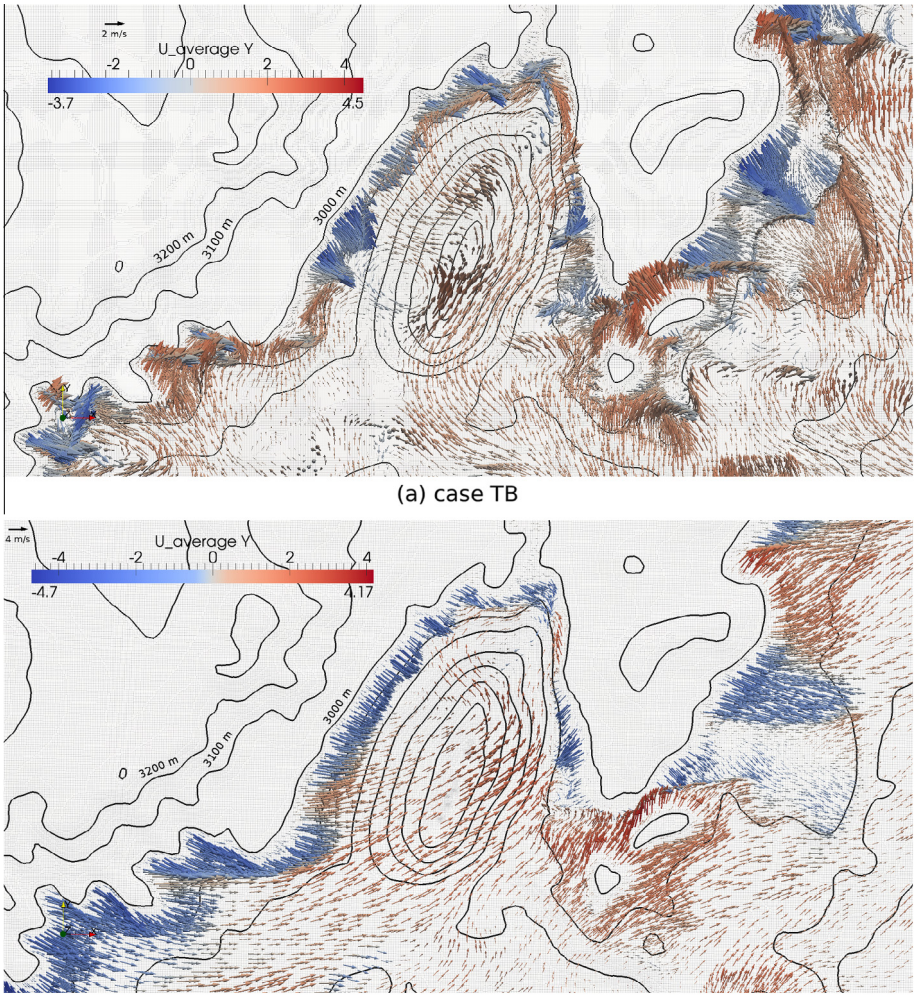

Fig. 13. Last hour mean velocity vector field in a horizontal plane at 3000 m. (a) Case TB, wind aloft 3 m/s. (b) Case TWB, wind aloft 10 m/s. Color bars associated to horizontal velocity component U_y, m/s. Topographic contour lines included. To improve visualization a different vector scale was used in each case, due to the difference in wind magnitude. (For interpretation of the references to color in this figure legend, the reader is referred to the web version of this article.)

Table 3
Mean vertical velocity ($\overline{W}$, m/s) and flux ($\overline{F}$, dam^3/s) at 250 m above the bottom of the pit, for each buoyant case simulated (B and WB, idealized geometry; TB and TWB, real topography). The horizontal plane inside the cavity was divided in two zones: an internal region, far from the walls of the pit, and a near-wall region, less than 150 m from the hillsides.

Region	Case							
	B		WB		TB		TWB	
	$\overline{W}$	$\overline{F}$	$\overline{W}$	$\overline{F}$	$\overline{W}$	$\overline{F}$	$\overline{W}$	$\overline{F}$
Near-wall	+0.67	+580	+0.85	+740	−0.55	−550	−0.40	−420
Internal	−0.38	−585	−0.51	−780	+1.06	+600	+0.83	+470

over the top edge of the pit (cases TB and TWB respectively), using a surface heat flux of 240 W/m^2 in both cases (boundary conditions are similar to those of the idealized cases, see Section 3.2). The time step was 0.01 s, necessary to keep a low Courant number near complex topography, where the mesh is refined, for a full simulation time of 4 h (reaching a statistically stationary flow). To determine whether the steady state was achieved we performed time statistics while the simulation was executing in order to test the evolution of the temporal means of velocity (time evolution of the moving-average of the velocity at different points inside the domain). Also, different final times have been tested to ensure that convergent time-averaged results were attained. As a reference for monitoring statistical convergence in LES simulations see for example [31]. In each non-idealized case around two and a half months of CPU time was necessary in Levque cluster, running in parallel in 32 cores (Intel(R) Xeon(R) CPU X5550 (Nehalem) 2.67 GHz).

4.3. Results

Fig. 12 shows the last hour mean velocity vector field in a vertical plane aligned with the main axis of the pit (tilted 15° from north, see Fig. 11), for the two cases simulated. The vector field shows intense convective upward currents inside the pit, that modify the air circulation over and around the mine. Also, the flow near the mine shows a south–north orientation (y-axis, Fig. 11), different from the imposed west–east mean flow (x-axis). The case TB shows stronger uplifts (maximum vertical velocity ~3 m/s in case TB, and ~2.4 m/s in case TWB), while case TWB shows a flow more aligned with the imposed main direction.

Fig. 13, showing the last hour mean velocity vector field in a horizontal plane near the top edge of the pit, is useful to explain the south–north orientation of the main flow near the mine. Near the pit, positive values of U_y (flow from the south) dominate the

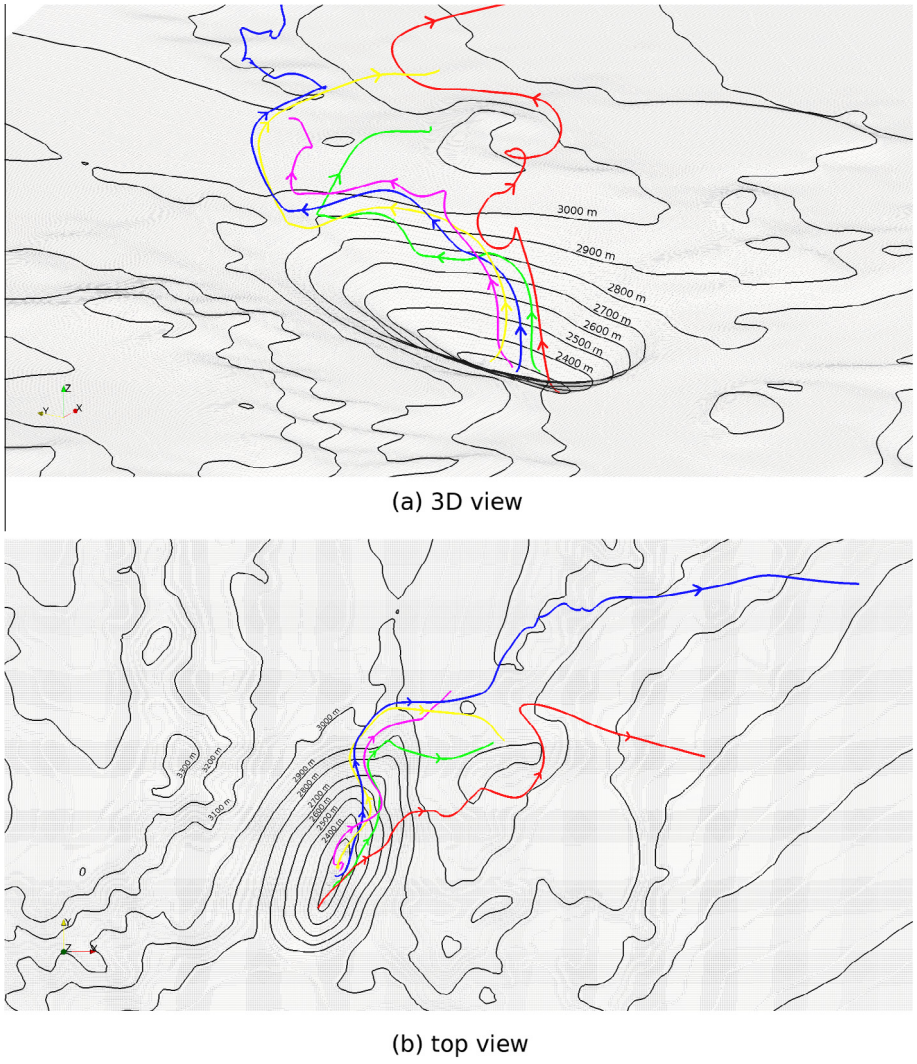

Fig. 14. Streamlines of the mean flow seeded from five points at 20 m above ground at the deepest zone inside the pit. Case TB, similar behavior at case TWB.

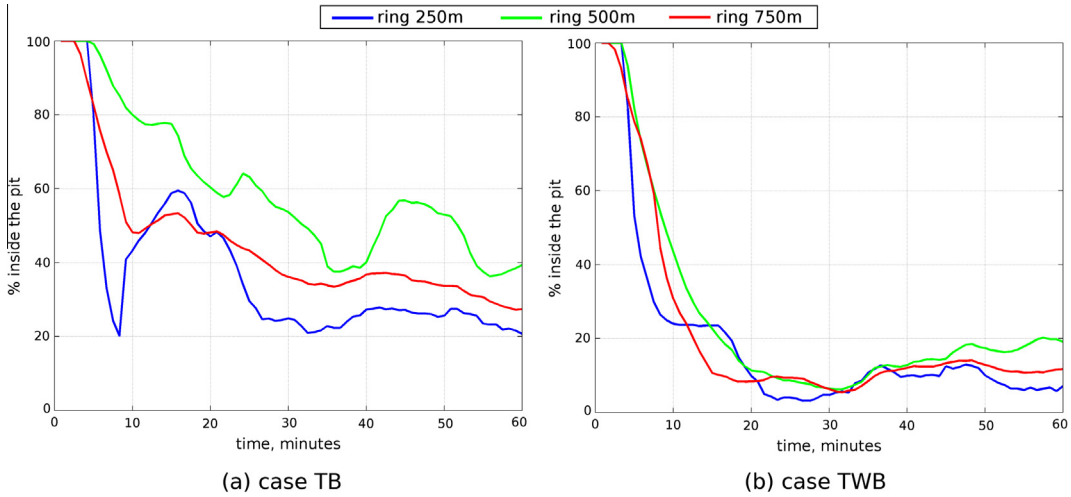

Fig. 15. Percentage of a puff of particles injected at a ring at different levels that remains inside the pit v/s time. (a) TB, (b) TWB. Blue line, particles injected at a ring 250 m above the bottom; green, ring at 500 m; red, ring at 750 m. (For interpretation of the references to color in this figure legend, the reader is referred to the web version of this article.)

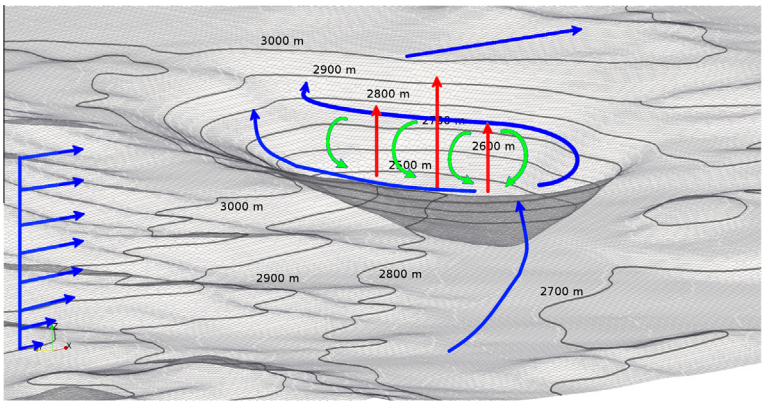

Fig. 16. Simplified conceptual scheme of flow circulation. Vectors are not at scale.

circulation, acting as a forcing for the flow entering the cavity, in both cases. This is so because the topography surrounding the pit forms a valley at its south, channeling the mean flow and forcing it to enter the pit through the lower level of the top edge. The flow configuration seen in Fig. 13 is similar to that seen in Fig. 3, near the top edge of the inverted cone used in the idealized simulations, with mean flow entering from the southwest. Strong convective updrafts are seen at the center of the pit in the case with real topography (maximum vertical velocity >2 m/s). These convective updrafts at the center of the cavity, far from walls, are also present in the idealized simulation (Fig. 3c), but with less intensity (maximum vertical velocity <1 m/s), probably due to the symmetric configuration of the ground and reduced extension of the main axis of the bottom surface. Both factors increase recirculation at the center of the pit and perturb the development of convective currents at that zone seen in the idealized cases. The high concentration and magnitude of convective updrafts seen at the center of the pit in Fig. 13 originate downward currents that descend over the contour of the mine.

In order to quantify the relative importance of internal and near-wall convective currents in each buoyant case, we computed the mean vertical velocity at 250 m above the bottom of the pit, dividing the horizontal plane inside the cavity in two zones: an internal region, far from the walls of the pit, and a near-wall region, less than 150 m from the hillsides. The results are shown in Table 3. As suggested by the vector fields in Figs. 3 and 12, clear differences between buoyant idealized cases (B and WB) and real cases (TB and TWB) exist. In idealized cases the mean value of vertical velocity is positive near the walls of the pit, due to high speed convective currents, and negative in the internal region, due to compensating subsidence. In cases with real topography, however, this configuration reverses, with positive mean vertical velocity far from the hillsides and negative close to them ($\overline{W}$ internal <0 in cases B and WB and >0 in cases TB and TWB). These results confirm the effect of the recirculatory flow, induced by the interaction of the wind that sweeps over the cavity and the internal atmosphere, on the vertical circulation inside the pit, fostering descending currents far from walls. In idealized cases stronger wind aloft (10 m/s in case WB, against 1 m/s in case B) increases both the negative value of internal mean velocity and the positive value of near-wall vertical mean velocity. In cases with real topography stronger wind aloft (10 m/s in case TWB, against 3 m/s in case TB) decreases both the positive value of internal mean vertical velocity and the negative value of near-surface mean vertical velocity. Also, the air flux ($\overline{F}$) is larger in case WB, where recirculation is more important. This confirms the previous idea of recirculation induced by the wind that sweeps the pit favoring descending currents inside its atmosphere, and evinces a link between wind aloft, geometry, recirculation and internal convective currents. In idealized cases the variation of the aspect ratio along the y-axis, caused by the circular geometry of the pit, induces recirculation inside the cavity, that inhibits the formation of upward currents inside the pit. In non-idealized cases the particular geometry of the pit, long and narrow, is aligned with the main direction of the flow, that is also channeled by the surrounding topography entering the pit through the lower levels of the top edge. Both factors increase the aspect ratio, reducing the recirculation, especially that linked to lateral walls in idealized cases. This increases the magnitude of internal updrafts, allowing the main flow to sweep the lateral hillsides of the pit.

Fig. 14 shows streamlines of the last hour mean flow seeded from five points at 20 m above ground at the deepest zone inside the pit. Convective currents leaving the basin are well depicted, and confirm the main role played by vertical upward currents inside the pit in the exit of particles from the mine in the cases that include topography. Also, the streamlines show the south–north flow dominating at low altitude over the pit, and the west–east mean flow controlling the circulation at higher altitudes (similar behavior in both cases simulated, only case TB shown).

In these complex-topography cases strong upward convective currents (vertical velocity >2 m/s) at the center of the cavity, induced by the particular topography of the pit, accelerate the exit of particles from the interior of the cavity. As in idealized cases, we injected particles inside the pit and studied their evolution (Fig. 15). The graphs show the percentage of particles remaining inside the pit v/s time. To simulate the generation of fugitive dust near the surface of the pit we injected a single puff of particles (at t = 3 h), at different locations: a 50 m-wide ring at 250 m above the bottom, that follows the surface of the slope of the pit (blue lines), a similar surface at 500 m (green lines) and another one at 750 m (red lines). In both cases a quick drop in the percentage of particles remaining inside the pit is seen. Even if the particles are injected near the walls they are quickly affected by internal convective updrafts. Since in this case the exit of particles is not controlled by upward currents near the walls, the level of the injection does not affect directly the percentage remaining inside the pit, as occurred in idealized cases. A quick change in the rate of discharge is seen after 10 min, with particles reentering the pit, especially those injected near the bottom of the cavity (blue lines in Fig. 15). This process is probably linked to downward currents associated to convective updrafts. The presence of strong interior convective updrafts (vertical velocity >2 m/s) explains the low percentage of particles remaining inside the pit, that in case TWB is even lower than those seen in idealized cases. Like in previous idealized cases, stronger wind in case TWB (10 m/s) increases the exit of particles.

4.4. Conceptual model

A simplified scheme of the flow is summarized in Fig. 16. The presence of an inlet valley modify the mean imposed wind, channeling the flow reaching the pit. As a consequence the flow sweeps the pit along its principal axis, and enters the cavity through the lower level of the top edge. This, together with the particular topography near the lower level of the pit, narrow in one axis and long in other, modifies the 3D aspect ratio of the cavity, reducing recirculation inside the pit, allowing the development of intense internal convective updrafts. Due to continuity, downward currents descend over the walls, at both sides of internal updrafts, where they interact with incident wind, that sweeps the lateral hillsides of the pit. The existence of intense internal convective currents and reduced recirculation inside the pit fosters the exit of particles from the mine and reduces their residence time inside its atmosphere.

5. Conclusions

We have applied a CFD solver to study the turbulent buoyant atmospheric flow inside large open pit mines under intense insolation, and its effect over pollutant dispersion. Using a DES approach we have incorporated buoyancy, stratification, developed turbulence and complex topography in our analysis. Three idealized cases were studied, and two full scale simulations using the complex topography of Chuquicamata were performed.

The simplified conceptual model of the air circulation seen in each case shows clear differences. In idealized case W, without buoyant currents, the main flow aloft induces recirculation inside the pit, while strong turbulence exists at the top of the pit (standard deviation of velocity magnitude $\sim$1.6 m/s), enhancing the exit of particles that reach that zone carried by ascending currents linked to the main roll. In idealized case B, dominated by buoyancy, strong convective currents (vertical velocity >2 m/s) near the walls dominate the flow, enhancing the exit of particles, while a descending flow is induced at the center of the cavity by continuity. Both previous schemes combine in idealized case WB, where intense convective currents near walls enhance the main roll inside the pit. In both cases with complex topography, TB and TWB, the inlet valley modifies the mean imposed wind, channeling the flow, that now sweeps the cavity along its principal axis, and enters the pit through the lower level of the top edge. This, together with the particular topography near the lower level of the pit, narrow in one axis and long in other, modifies the 3D aspect ratio of the cavity, reducing recirculation inside the pit, allowing the development of intense internal convective updrafts.

The results of this work point to the key role played by buoyant currents fostering the dispersion of contaminants inside and outside large open pit mines under intense insolation: despite the large size of the pit considered, in all cases buoyant currents contribute to the exit of a large percentage of the particles injected inside the pit. In particular, buoyancy modifies the flow patterns that the purely mechanically-induced recirculation generates inside the pit, reducing the particle residence time seen in the purely mechanical case (non-buoyant case). The different cases studied, with and without a complex topography, also shed light in the role of geometry in the flow patterns, especially in flow recirculation. Given that the aspect ratio of the cavity controls the intensity and location of the main roll inside the pit, idealized cases, with a circular geometry that produces a reduction of the aspect ratio along the axis perpendicular to the main flow, show intense recirculation inside the pit, even in cases with strong buoyancy (surface heat flux $\sim$240 W/m^2). Non-idealized cases, on the other hand, have an inlet valley that aligns the main flow with the main axis of the cavity, forcing it to enter the cavity through the lower level of the top edge, and have a non circular geometry that is aligned with the main flow. Both factors highly increase the aspect ratio, reducing the recirculatory flow induced mechanically inside the pit, that is now unable to overcome the intense buoyant currents at the center of the cavity. Anyhow, whether by internal or near wall upward currents, in all buoyant cases considered a large percentage of the particles injected inside the pit leaves the cavity after 30 min. Idealized cases also showed that recirculation contributes to the re-entry of particles at the top edge, reducing the exit of particles.

Further experiments studying the effect of 3D aspect ratio over the mechanically forced internal flow are needed to understand the precise effect of the internal geometry of the pit over the flow. As reported in this work, this is particularly important considering the variations of the cavity aspect ratio along the axis perpendicular to the main flow seen in large scale open pit mines.

The present work may give more insight into the complex patterns of circulation that affect Chuquicamata, allowing the study of measures to minimize the effect of fugitive dust over the operations. Also, a similar framework as the one presented here can be used to study similar large scale atmospheric flows that include complex topography, developed turbulence, stratification and buoyancy, such as dispersion of contaminants in urban environments, or wind energy studies.

Acknowledgements

This work was carried out during the doctoral research of the first author, with the support of Conicyt under Grant "Beca para Estudios de Doctorado Nacional". "René Garreaud was partially supported by FONDAP-CONICYT 15110009." *Powered @ NLHPC*: This research was partially supported by the supercomputing infrastructure of the NLHPC (ECM-02), Center for Mathematical Modeling CMM, Universidad de Chile.

Appendix A. Supplementary material

Supplementary data associated with this article can be found, in the online version, at http://dx.doi.org/10.1016/j.compfluid.2013.11.012.

References

[1] Baklanov A. Numerical modelling of atmosphere processes in mountain cirques and open pits. Air Pollut III: Air Pollut Theory Simul 1995:1.
[2] Baklanov A. Application of CFD methods for modelling in air pollution problems: possibilities and gaps. J Environ Monit Assess 2000;65:181–90.
[3] Baklanov A, Rigina OY. Research of local zones atmosphere normalization efficiency by artificial currents. Trans Ecol Environ 1995:3.
[4] Rigina O, Baklanov A. Numerical modelling of dispersion of dust-gas plume in the atmosphere after mass explosions. Trans Ecol Environ 1995:6.
[5] Shi Y, Feng X, Wei F. Three-dimensional nonhydrostatic numerical simulation for the PBL of an open-pit mine. Boundary-Layer Meteorol 2000;94:197–224.
[6] Silvester S, Lowndes I, Hargreaves D. A computational study of particulate emissions from an open pit quarry under neutral atmospheric conditions. Atmos Environ 2009;43:6415–24.
[7] Bres G, Colonius T. Three-dimensional instabilities in compressible flow over open cavities. J Fluid Mech 2008;599:309–39.
[8] Kang W, Sung HJ. Large-scale structures of turbulent flows over an open cavity. J Fluids Struct 2009;25:1318–33.
[9] Mesalhy O, Aziz SSA, El-Sayed MM. Flow and heat transfer over shallow cavities. Int J Therm Sci 2009;49:514–21.
[10] Wyngaard JC. Toward numerical modeling in the "Terra Incognita". J Atmos Sci 2004;61:1816–26.
[11] Chen F, Kusaka H, Bornstein R, Ching J, Grimmond C, Grossman-Clarke S, et al. The integrated WRF/urban modeling system: development, evaluation, and applications to urban environmental problems. Int J Climatol 2011;31:273–88.
[12] Flores F, Garreaud R, Muñoz R. CFD simulations of turbulent buoyant atmospheric flows over complex geometry: solver development in OpenFOAM. Comput Fluids 2013;82:1–13.

[13] Spalart PR, Jou W, Strelets M, Allmaras SR. Comments on the feasibility of LES for wings, and on a hybrid RANS/LES approach. In: Proceedings of 1st AFOSR international conference on DNS/LES; 1997. p. 137–47.
[14] Spalart PR. Detached-eddy simulation. Ann Rev Fluid Mech 2009;41:181–202.
[15] Kiefer MT, Zhong S. A numerical modeling study of the nocturnal boundary layer inside Arizona's Meteor Crater. In: 19th Symposium on boundary layers and turbulence, 12 April 2010. American Meteorological Society; 2010.
[16] Fritts DC, Goldstein D, Lund T. High-resolution numerical studies of stable boundary layer flows in a closed basin: evolution of steady and oscillatory flows in an axisymmetric arizona meteor crater. J Geophys Res 2010;115. D18109–.
[17] Sharples J, McRae R, Weber R. Wind characteristics over complex terrain with implications for bushfire risk management. Environ Model Softw 2010;25:1099–120.
[18] Skyllingstad ED. Large-eddy simulation of katabatic flows. Boundary-Layer Meteorol 2002;106:217–43.
[19] Axelsen SL. Large-eddy simulation and analytical modelling of katabatic winds. Ph.D. thesis, Institute for Marine and Atmospheric research, Faculty of Science, Department of Physics and Astronomy, Utrecht University, The Netherlands; 2010.
[20] Whiteman CD. Observations of thermally developed wind systems in mountainous terrain. Atmos Process Complex Terrain Meteorol Monogr 1990:1–4.
[21] Colette A, Chow FK, Street RL. A numerical study of inversion-layer breakup and the effects of topographic shading in idealized valleys. J Appl Meteorol 2003;42:1255–72.
[22] Whiteman CD, Muschinski A, Zhong S, Fritts D, Hoch SW, Hahnenberger M, et al. METCRAX 2006 meteorological experiments in Arizona's Meteor crater. BAMS, American Meteorological Society; 2008.
[23] Issa R. Solution of the implicitly discretised fluid flow equations by operator-splitting. J Comput Phys 1985;62:40–65.
[24] Issa R, Gosman A, Watkins A. The computation of compressible and incompressible recirculating flows by a non-iterative implicit scheme. J Comput Phys 1986;62:66–82.
[25] Oliveira P, Issa R. An improved PISO algorithm for the computation of buoyancy-driven flows. Numer Heat Transfer 2001;Part B, 40:473–793.
[26] Demirdzic I, Lilek Z, Peric M. A collocated finite volume method for predicting flows at all speeds. Int J Numer Methods Fluids 1993;16:1029–50.
[27] Maureira JC, Baeza C, Pérez T. Levque cluster user manual. Universidad de Chile; 2011. Major scientific and technological equipment for user facility centers.
[28] Moeng CH, Sullivan P. A comparison of shear -and buoyancy- driven planetary boundary layer flows. J Atmos Sci 1994;51(7):999–1022.
[29] Churchfield M, Moriarty P, Vijayakumar G, Brasseur J. Wind energy-related atmospheric boundary layer large-eddy simulation using openfoam. In: 19th Symposium on Boundary layers and turbulence, Keystone, Colorado, August 2–6, 2010; 2010.
[30] de Villiers E. The potential of large eddy simulation for the modeling of wall bounded flows. Ph.D. thesis; Thermofluids Section, Department of Mechanical Engineering, Imperial College of Science, Technology and Medicine; 2006.
[31] Gousseau P, Blocken B, van Heijst G. Quality assessment of large-eddy simulation of wind flow around a high-rise building: validation and solution verification. Comput Fluids 2013;79:120–33.
[32] Batchelor GK. An introduction to fluid dynamics. Cambridge University Press; 1967.
[33] Schlichting H. Boundary-layer theory. McGraw Hill; 1979.
[34] Barkan J, Alpert P. The linkage between solar insolation and dust in the major world deserts. Open Atmos Sci J 2010;4:101–13.
[35] Garreaud R. The Andes climate and weather. Adv Geosci 2009;7:1–9.
[36] Rutllant J, Fuenzalida H, Aceituno P. Climate dynamics along the arid northern coast of Chile: the 1997–1998 Dinámica del Clima de la Región de Antofagasta (DICLIMA) experiment. J Geophys Res 2003;108. 4538–.
[37] Garreaud RD, Rutllant JA, Muñoz RC, Rahn DA, Ramos M, Figueroa D. VOCALS-CUpEx: the Chilean upwelling experiment. Atmos Chem Phys 2011;11:2015–29.